nature communications

Article

https://doi.org/10.1038/s41467-024-54641-z

Noninvasive rejuvenation strategy of nickel-rich layered positive electrode for Li-ion battery through magneto-electrochemical synergistic activation

Received: 3 May 2024

Accepted: 14 November 2024

Published online: 26 November 2024

Check for updates

Haochen Gong[1], Yu Cao[1], Baoshan Zhang[2], Jinsong Zhang[3], Yiming Zhang[1], Huili Wang[1], Shaojie Zhang[1], Xiaoyi Wang[1], Yue Mao[1], Shuo Liu[1], Chengyu Han[1], Qianxin Xiang[4], Chaoyi Zhou[4] & Jie Sun[1,2]

Nickel-rich layered oxides are one of the most promising positive electrode active materials for high-energy Li-ion batteries. Unfortunately, the practical performance is inevitably circumscribed by the structural deterioration deriving from the Ni/Li antisite disorder, leading to severe capacity loss and life attenuation. Herein, we propose an economical and facile rejuvenation strategy by employing the magneto-electrochemical synergistic activation targeting the positive electrode in assembled Li-ion batteries. This approach induces a transition of Ni^{3+} from high-spin to low-spin, reducing the super-exchange interaction of Ni-O-transition metal (TM). Meanwhile, electrochemical reaction drives Li^{+} from the host material and promotes Ni^{3+} to reoccupy TM layer, recovering intrinsic Li site and extending cycle life. The strategy demonstrates that low-quality positive electrodes can be converted to high-quality ones. Notably, the method can revitalize an aged Li-ion pouch cell (SiC||NCM811, 8 Ah nominal capacity) via optimizing cation occupancy and increase its capacity by 10% from 6.49 to 7.14 Ah at 1 C, illustrating the benefits of the upcycling process.

With the mounting demand of large-scale energy storage devices and long-range electric vehicles, it is urgent to develop Li-ion batteries with superior energy and power densities[1,2]. Researchers have focused the target on exploring electrode materials with high specific capacity, especially positive electrode materials, which account for both the dominating mass and budget proportion in batteries[3,4]. Compared with numerous positive electrode materials, layered lithium nickel–cobalt–manganese oxides ($LiNi_xCo_yMn_{1-x-y}O_2$, denoted as NCM hereafter) have been verified as one of the most prospective positive electrode candidates, which have been applied to power battery market[5]. In order to further obtain the ever-increasing specific energy (>300 Wh/kg_{cell}), the development of nickel-rich NCM ($x \geq 0.8$) is imperative, attributing to its high specific capacity (>250 mAh/g), excellent dynamic performance and relative low budget[2]. Nevertheless, an increased nickel content is associated with a heightened risk of Ni/Li antisite disorder within the bulk material[6–9], (as detailed in Supplementary Table 1). This disorder exacerbates the degradation of phase transition during electrochemical reactions, which is a critical issue that warrants further investigation[10].

Numerous research works have been done to optimize the synthesis conditions and obtain high-quality crystals[11–14], however, the initial Ni/Li antisite disorder is inevitable in nickel-rich NCM

[1]School of Chemical Engineering and Technology, Tianjin University, Tianjin, China. [2]Quzhou Institute for Innovation in Resource Chemical Engineering, Quzhou, Zhejiang, China. [3]State Key Laboratory of Low-Dimensional Quantum Physics, Department of Physics, Tsinghua University, Beijing, China. [4]Guizhou Zhenhua E-Chem Co., Ltd, Guiyang, China. e-mail: jies@tju.edu.cn

containing a large number of trivalent nickel ions[15–17]. As is well known, the reason for the Ni^{2+}/Li^{+} antisite disorder is due to their similar ionic radii. In addition, Li^{+} are also prone to exchange with Ni^{3+}[18], alleviating the magnetic frustration. The strong interlayer coupling between the migrated nickel in Li site and another adjacent transition metal (TM) in the TM layer generates the super-exchange interaction which is bridged by one oxygen ion (labeled as Ni–O–TM)[19]. This super-exchange interaction is generally strong, leading to the inevitable disordered arrangement configuration[2,20,21], which will be aggravated in charging/discharging process, thereby resulting in irreversible crystal phase transformation and structural collapse. The accordingly evolution of the surface can significantly influence the side reaction dynamics at the cathode|electrolyte interface (CEI)[22].What's worse, the nickel ions in Li layer are easily dissolved into electrolyte[13].

It is recently reported that the more unpaired electrons in 3*d* orbitals of the TM ions located on both sides of oxygen, the stronger 180° linear super-exchange interaction exists, thus the higher Ni/Li antisite disorder will occur[15,23,24]. Because the super-exchange interaction and the disorder depend on the electron spin state of Ni, it is utmost important but not clear yet how to tune it for optimizing the lithiation/delithiation behavior. It is crucial to conduct in-depth research on the fundamental principles of electron spin states in electrochemical reaction processes. Understanding the influence of these principles on Ni/Li antisite disorder and its resultant effects on electrochemical performance is crucial for advancing our knowledge in this field.

Herein, we elucidated that the deterioration of Ni/Li antisite disorder in $LiNi_{0.8}Co_{0.1}Mn_{0.1}O_2$ (NCM811) during the electrochemical reaction process is concomitant with an elevation in high-spin state of Ni^{3+} (as depicted in Fig. 1). The increase in high-spin state facilitates the migration of Ni^{3+} into Li site, driven by the strong super-exchange interaction among the high-spin Ni^{3+} in Li layer (antisite Ni^{3+}), O^{2-} and the adjacent TM. During the electrochemical lithiation/delithiation process, NCM811 exists in a metastable state accompanied by lattice distortion, leading to the alterations of d-electron energy level in TM. Concurrently, the associated redox reactions induce changes in the d-electron pairing and splitting states of Ni^{3+}, which is the reason why the high-spin state of Ni^{3+} increases upon cycling. Based on this theory, we introduced an external magnetic field during the electrochemical activation process. This intervention modulates the re-pairing state of d-electrons through Zeeman effect, which regulates the spin-electron energy[25]. The application of external magnetic field effectively mitigates Ni/Li antisite disorder and promotes an ordered rearrangement in NCM811 crystal. This "rejuvenation" is achieved by strategically manipulating Ni^{3+} to low-spin configuration, which diminishes super-exchange interactions and bolsters the overall stability of the material. Intriguingly, the implementation of the "rejuvenation" strategy during the initial electrochemical activation yielded a remarkable outcome: the Ni/Li antisite disorder in the activated NCM811 was unexpectedly reduced, even falling below that of the pristine material. As a result, the graphite||NCM811 pouch cell (2 Ah) demonstrates practicable performance, delivering a high initial Coulombic efficiency (ICE) of 90.64%. Moreover, after 1000 cycles, it maintains an 89.21% capacity retention

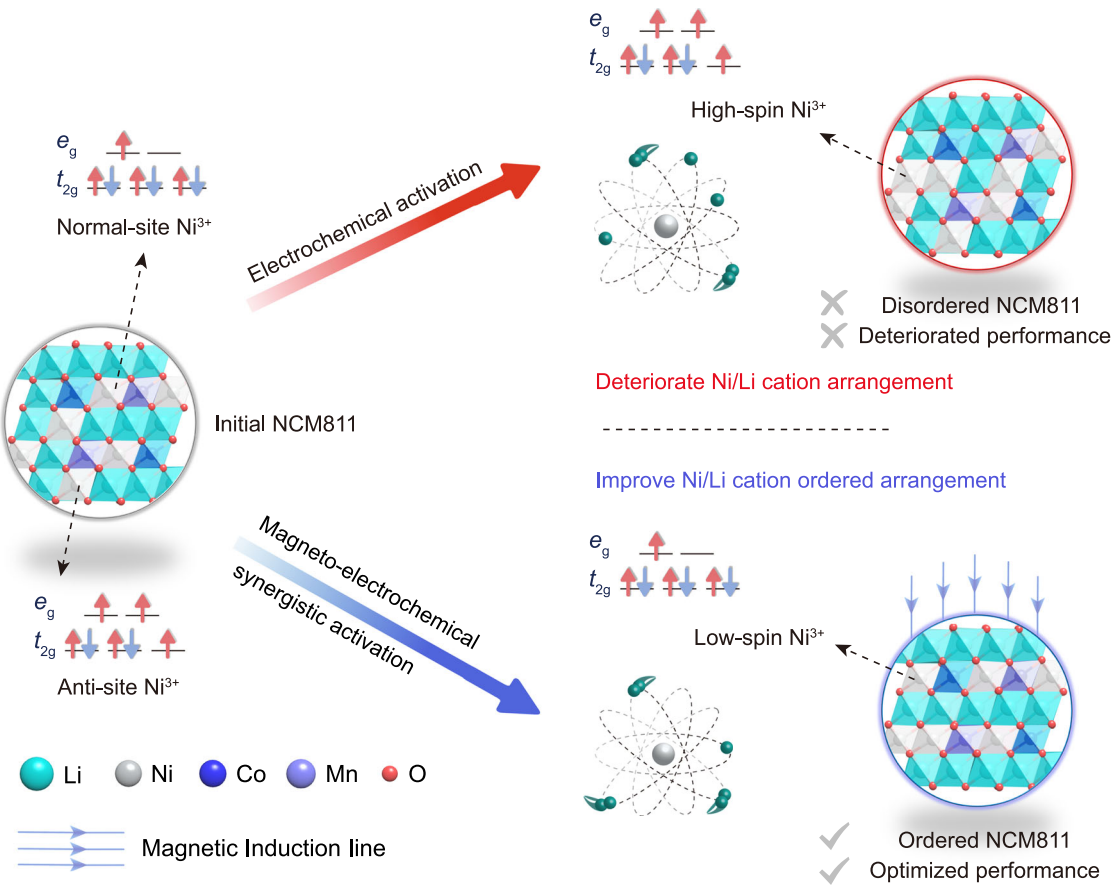

Fig. 1 | The proposed mechanism of the magneto-electrochemical synergistic activation (MEA) in the graphite||NCM811 battery. Schematic of proposed mechanism of MEA effect on NCM811 electrode. When NCM811 was applied in electrochemical activation, the content of high-spin Ni^{3+} increased, leading to Ni/Li antisite disorder and degraded electrochemical performance due to the strong super-exchange interaction. When employing the MEA strategy, Ni^{3+} transition to a low-spin state. This strategic intervention further realizes the ordered rearrangement of Ni/Li cations within the material, enabling the enhancement and efficient upcycling of NCM811.

at 0.5 C. Additionally, when the "rejuvenation" strategy was performed in the spent batteries for five cycles, the Ni/Li antisite disorder degree in the rejuvenated NCM811 was significantly reduced. In essence, the magneto-electrochemical synergistic activation (MEA) is a energy-saving and eco-friendly "rejuvenation" strategy, which can effectively transform the inferior materials into those with superior properties. This finding suggests that the strategy is amenable to repeated applications, potentially leading to a substantial prolongation of the battery's service life.

Results

Regulation of electron spin in NCM811

The MEA process rejuvenates NCM811 through the application of the magnetic field, which is generated by parallel electromagnets as depicted in Fig. 2a, b, during the electrochemical reactions of Li-ion batteries. The field emanates from the north pole to the south pole, ensuring a uniform and robust magnetic field established between the pole caps. The magnetic field is oriented along the axial direction of the pole caps, perpendicularly traversing the battery's positive and negative electrodes. The intensity is precisely controlled by tuning the output power and the distance between the magnetic poles. Coin or pack cells positioned between two magnets were subjected to activate and rejuvenate in the magnetic field.

The spin state of Ni^{3+} was characterized using the magnetic property measurement system (MPMS), and the corresponding results were delineated by the temperature dependence of inverse magnetic susceptibilities. We obtained the total effective magnetic moment (μ_{eff}) of NCM811 samples with various battery activation conditions (Fig. 2c). Based on the μ_{eff}, the $\mu_{Ni^{3+}}$ in NCM811 and the ratio of high and low-spin states, respectively, can be calculated according to the measured values by giving the magnetic moment contribution of Co^{3+} and Mn^{4+} (see Supplementary part 1 for detailed calculation)[26]. In the fresh NCM811, the high-spin Ni^{3+} accounts for 80.48% of the total Ni^{3+}. In different magnetic field intensities, with all cathodes in the discharged state, the proportion of high-spin Ni^{3+} is 87.29% at 0 T, 67.84% at 0.08 T, 43.49% at 0.16 T, and 19.85% at 0.32 T, respectively (Fig. 2d). It suggests that partial Ni^{3+} transform into high-spin state during the electrochemical activation without magnetic field, leading to the enhanced super-exchange interaction of Ni–O–TM and an abominable Ni/Li antisite disorder. Surprisingly, in the presence of magnetic field, the unpaired electron number of octahedral coordinated Ni^{3+} decreased from 3 ($t_{2g}^5e_g^2$, high-spin state) to 1 ($t_{2g}^6e_g^1$, low-spin state). Furthermore, with the increase of magnetic field strength, the proportion of low-spin state Ni^{3+} in NCM811 increased during the MEA process. The findings conclusively demonstrate that the MEA effectively modulates the spin state of Ni^{3+} in NCM811.

In the end of the conventional electrochemical activization, most Ni^{3+} in NCM811 at discharged state performs a high-spin state with three unpaired electrons in e_g and t_{2g} orbitals. The e_g orbital of each antisite Ni^{3+} (in Li layer) connects to the nearest TM in the TM layer through the adjacent O^{2-} with p orbital, forming the Ni^{3+}–O^{2-}–TM coordination configuration with a 180° linear σ bond, which is always

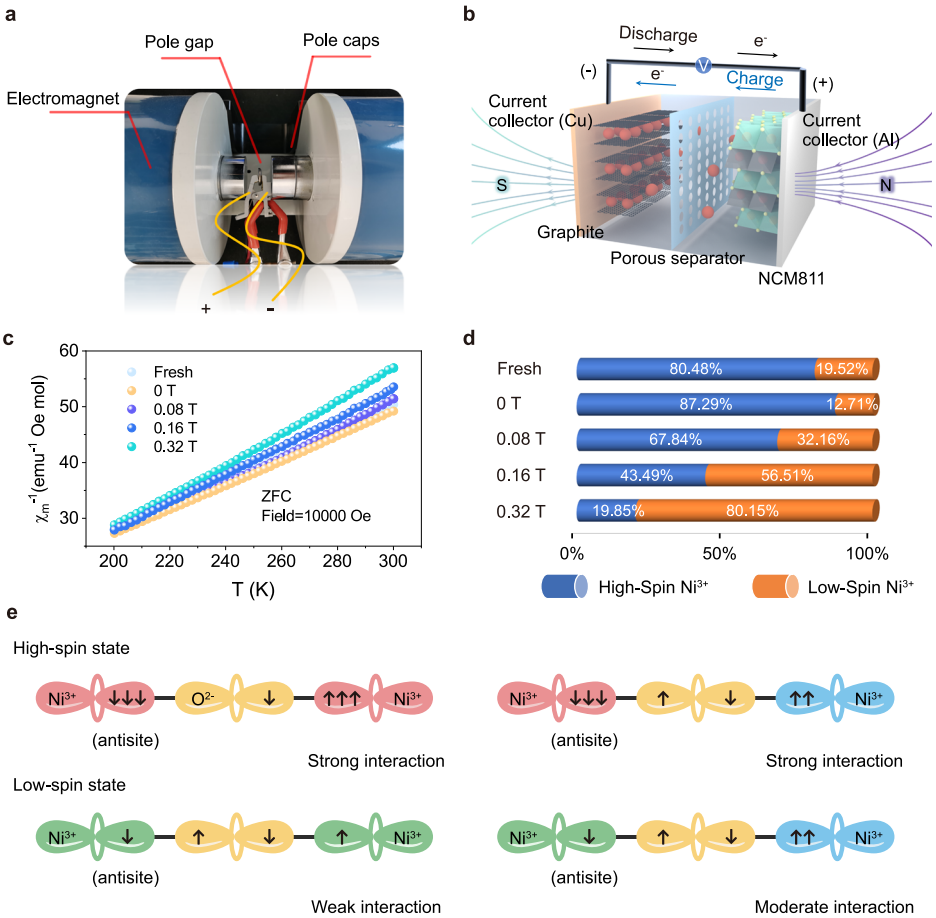

Fig. 2 | MEA method for batteries and the magnetism characterization. a, **b** The device and the schematic of MEA for the graphite||NCM811 battery. The generation and intensity of magnetic field can be controlled by an external direct current power supply. **c** Temperature dependence inverse susceptibilities of NCM811 samples in lithiated state with various activation conditions. **d** Proportions of high and low-spin states Ni^{3+} with various activation conditions calculated from (**c**). **e** Schematic of the Ni^{3+} related super-exchange interaction in different spin states. High-spin Ni^{3+} ions typically engender robust super-exchange interactions, whereas the configuration of low-spin Ni^{3+} ions result in diminished super-exchange interactions.

strong due to the high-spin state of Ni^{3+}, resulting in the formation of strong super-exchange interaction (Fig. 2e) and the occurrence of Ni/Li antisite disorder[15,27,28]. The minimum proportion of high-spin Ni^{3+} can be obtained by applying a 0.32 T magnetic field, indicating that the unpaired electrons of e_g orbital in high-spin Ni^{3+} transfer to t_{2g} orbital, and Ni^{3+} changes to low-spin state. Accordingly, the weakened super-exchange interaction (low-spin Ni^{3+}–O^{2-}–TM) suppresses Ni^{3+}/Li^{+} antisite disorder during charging/discharging processes. It indicates that the magneto-electrochemical synergistic effect can alleviate the super-exchange interaction and is beneficial to reduce the Ni/Li antisite disorder degree.

Structural evolution of NCM811

The crystal configuration parameters and the precise Ni/Li antisite disorder ratio of NCM811 are refined and calculated by the X-ray diffraction (XRD) Rietveld method (Supplementary Note 1). The original state of the NCM811 has a Ni/Li antisite disorder ratio of 4.93%. The ratio irreversibly increases to 5.02% after the initial electrochemical activation (Fig. 3a), due to the strong super-exchange interaction as discussed above. After the electrochemical activation, the invasion of antisite atoms will lead to the formation of disordered TM layer, consequently causing a degradation in performance[8,29]. On the contrary, when the initial electrochemical activation of the graphite||NCM811 battery was performed in 0.32 T magnetic field (Fig. 3b), the Ni/Li antisite disorder ratio significantly decreased to 1.80% at the charged state (3.7 V) and 1.85% at the discharged state (3.0 V), respectively. Furthermore, the interlayer space of the NCM811 exhibited a pronounced expansion (Supplementary Fig. 1), indicating the ordered rearrangement of Ni/Li ions and well-ordered layer structure by magneto-electrochemical synergistic effect.

To further investigate the dynamic evolution of Ni/Li antisite disorder arrangement in NCM811 during MEA with 0.32 T magnetic field, the ex situ XRD at different charged and discharged states are characterized in Fig. 3c. The intensity ratio of (003) and (104) peak varies obviously in reaction process and can be considered as the characteristic of the order degree of NCM811. The small (003)/(104) ratio represents the high Ni/Li antisite disorder degree[30–32]. With the MEA proceeding, the (003)/(104) ratio first gradually increases, reaching the extreme value at 3.7 V, then decreases as charging to 4.3 V, but it keeps increasing during the following discharge process. Accordingly, the Ni/Li antisite disorder degree reached 1.85% after the first cycle by MEA, which is much lower than that of the original state (4.90%), indicating that the rejuvenated NCM811 can be obtained.

Figure 3d illustrates the trend in Ni/Li antisite disorder across the whole MEA proceeding (the original and refinement data are shown in Supplementary Figs. 2–4 and Supplementary Table 2). During the initial charging process (OCV to 3.7 V), a large amount of Ni^{3+} in NCM811 can be tuned as a low-spin state (Fig. 2d and Supplementary Fig. 5), causing the diminished super-exchange interaction and the migration of low-spin Ni^{3+} back into TM layer, thereby releasing additional Li sites. When it was charged to the high-voltage range of 3.7–4.0 V, with the removal of a large amount of lithium, the Ni ions migrated back to TM layer were basically saturated, resulting in the highly occupation of Ni in TM layer. As for the tetravalent nickel ion can be generated above 4.0 V at the deeply delithiated state, it possessed diverse electron orbital configurations ($t_{2g}^6e_g^0$, $t_{2g}^5e_g^1$, $t_{2g}^4e_g^2$) and showed a high activity, leading to the continuous invasion of Ni^{4+} into the vacancies in Li layer.

In the following discharging process (from 4.3 to 3.8 V), the migration of Ni ions was influenced by two kinds of opposite effects. The gradually increased lithium concentration, as a positive effect, can repel the unstable nickel ions in Li sites back to TM layer. In contrast, the strong super-exchange interaction of Ni^{4+}–O–TM will aggravate antisite disorder arrangement. The interaction of these two effects results in the slow migration of nickel ions back to TM layer. Until discharging below 3.8 V, the degree of Ni/Li antisite disorder shows a landslide downward trend, due to that the large amount of Ni^{3+} is reformed and exists in low-spin state ($t_{2g}^6e_g^1$) in the magnetic field, resulting in the weakened super-exchange interaction, the suppressed Ni/Li antisite disorder and the shipshape layered structure.

In the fully lithiated state of NCM811, the spin states of Co^{3+} ($t_{2g}^6e_g^0$) and Mn^{4+} ($t_{2g}^3e_g^0$) are constant due to their empty e_g orbitals, ensuring that the localized electronic configuration in their t_{2g} orbitals and the associated energy coincide with their initial values by the end of the MEA process. During the activation process, the magnetic field modulated the spin state of nickel ions and attenuated the super-exchange interaction, meanwhile electrochemical reaction facilitates the extraction of lithium ions from the host material and prompts the reintegration of nickel ions into the TM layer. To verify the magneto-electrochemical synergistic effect, we subjected NCM811 powder to a uniform magnetic field in the absence of electrochemical reactions for about 20 h. The experiment analysis revealed no significant alterations in the Ni/Li antisite disorder compared with the initial state (Supplementary Fig. 6). Consequently, it is inferred that the orchestrated rearrangement of Ni/Li ions within NCM811 is predominantly governed by the synergistic effects of magneto-electrochemical interactions. In addition, XRD and electron paramagnetic resonance (EPR) spectroscopy indicate that the NCM811 by MEA sustains a relatively low Ni/Li antisite disorder over the subsequent 300 cycles (Supplementary Figs. 7 and 8), suggesting that a well maintenance of initial ordered layered structure is the key factor to restrain the continuous degradation of NCM811.

We further calculated Ni/Li antisite disorder energy with a specified magnetic spin orientation using ab initio calculations. Figure 3e exhibits the disorder energies of Ni^{3+} and Li^{+} with zigzag sites in NCM811, which are 0.88 eV in magnetic field and 0.63 eV without magnetic field, respectively. It indicates that the antisite disorder is effectively inhibited by applying a given magnetic field. In addition, the rearrangement energy barrier (ΔE) of Ni^{3+} from Li layer back to TM layer is 2.69 eV by MEA. This value is substantially lower than that observed during conventional electrochemical activation (3.49 eV), indicating that the imposition of a magnetic field significantly enhances the kinetic dynamics associated with the ordered rearrangement of nickel and lithium ions. A schematic elucidating the influence of the Ni^{3+} spin state on the local atomic structure is shown in Supplementary Fig. 9.

Electrochemical performance

To clarify the MEA behaviors, cyclic voltammetry (CV) curves were tested in the initial oxidation–reduction process. As shown in Fig. 4a, the anodic peak at 3.736 V in the first cycle is observed in 0.32 T MEA battery, corresponding to the delithiation combined with the oxidation of Ni^{2+}, which is slightly prior to the one without magnetic field (3.792 V, Fig. 4b). This is attributed to the higher Ni/Li orderliness obtained by rearranging Ni into the TM layer. The well-ordered structure brings about the reduced polarization of battery from 0.204 V to 0.149 V. After the MEA process, the decreased voltage hysteresis in CV curves for the second cycle also indicates the promoted Li-ion diffusion and delithiation dynamics, due to the magnetohydrodynamic effect[33,34]. The galvanostatic intermittent titration technique analysis revealed fast kinetics closely related to the Li^{+} diffusion (Supplementary Fig. 10). After the initial 0.32 T MEA, the average ion diffusion coefficients of Li^{+} ($D_{Li^{+}}$) at 0.1 C all over the different charging states is 6.34×10^{-10} cm^2 s^{-1}, which is much higher than that of 0 T MEA battery (1.39×10^{-10} cm^2 s^{-1}), as shown in Fig. 4c. The ordered ionic arrangement significantly enhanced the Li^{+} diffusion in NCM811.

The influence of magnetic field intensity on electrochemical performance was tested in Fig. 4d. Among all the conditions in 0, 0.08, 0.16, 0.32 and 0.64 T magnetic fields, the 0.32 T MEA battery exhibits the optimal electrochemical performance. Moreover, in the intensity

https://doi.org/10.1038/s41467-024-54641-z

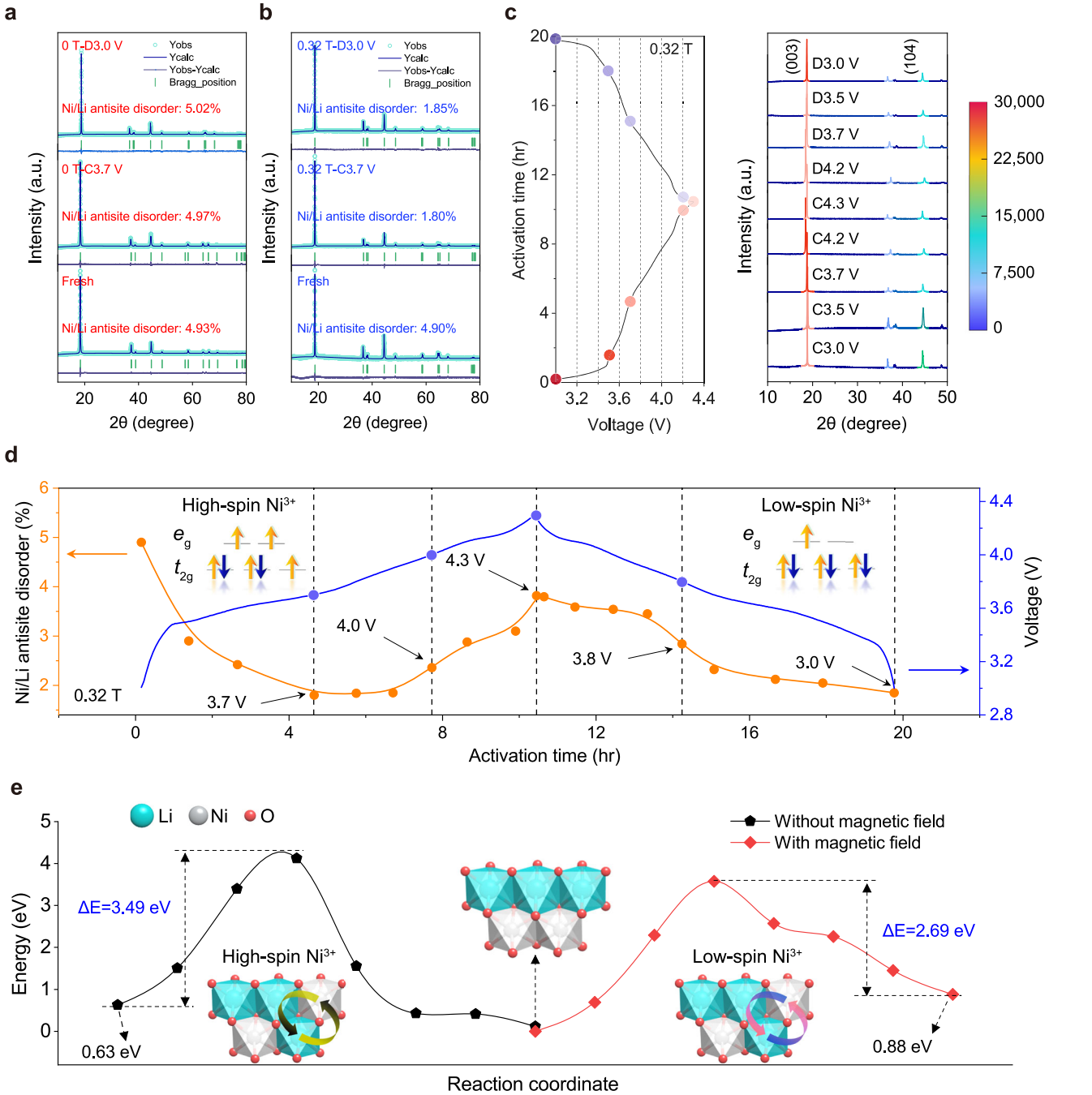

Fig. 3 | XRD characterization and rejuvenation for layered oxide in the graphite||NCM811 full battery. a, **b** Rietveld refinement results of NCM811 at the initial state, charged state (3.7 V) and discharged state (3.0 V) during the activation process with the magnetic field of 0 T (**a**) and 0.32 T (**b**) in the graphite||NCM811 full battery. **c** Activation-voltage curve and X-ray diffractograms of various state of NCM811 electrodes. **d** The corresponding transformation of Ni/Li antisite disorder ratio in the MEA of 0.32 T magnetic field. **e** Ni/Li antisite disorder energies and the rearrangement energy barriers with or without magnetic field.

range of 0–0.32 T, a distinct positive correlation is observed between the battery's performance and the magnetic flux density. This relationship underscores the potential influence of magnetic fields on the cation site occupancy of positive electrode materials, suggesting that MEA is conducive to heal the original defects of Ni/Li antisite disorder in NCM811. As the intensity gradually ascends to 0.64 T, the battery performance rapidly decays and the ICE is only 72.4%. Once the magnetic flux density surpasses a critical threshold, an abrupt escalation in the battery's temperature is observed (Supplementary Fig. 11 and Supplementary Table 3). This phenomenon is attributed to the thermal effects induced by electromagnets, which can ultimately lead to a significant decline in the cycle life of the battery. Therefore, when the initial MEA process was performed in 0.32 T magnetic field, the graphite||NCM811 full battery provided a prominent reversible capacity of 189.4 mAh g^{-1} after 300 cycles at 0.5 C (100 mA g^{-1}) with an average coulombic efficiency of 99.84%, much higher than that in the control sample (0 T).

The ICE of graphite||NCM811 full cell (0.32 T) can reach up to 90.64%, which is much higher than that of the control cell (0 T, 82.90%), indicating a considerable reversible capacity enhancement (Fig. 4e and Supplementary Fig. 12). The low ICE of the latter is because that Ni ions invade into lithium layer and occupy lithium-storage sites.

We further scrutinized the MEA ability in a 2.0 Ah pouch cell, which was assembled with high mass loading NCM811 positive

https://doi.org/10.1038/s41467-024-54641-z

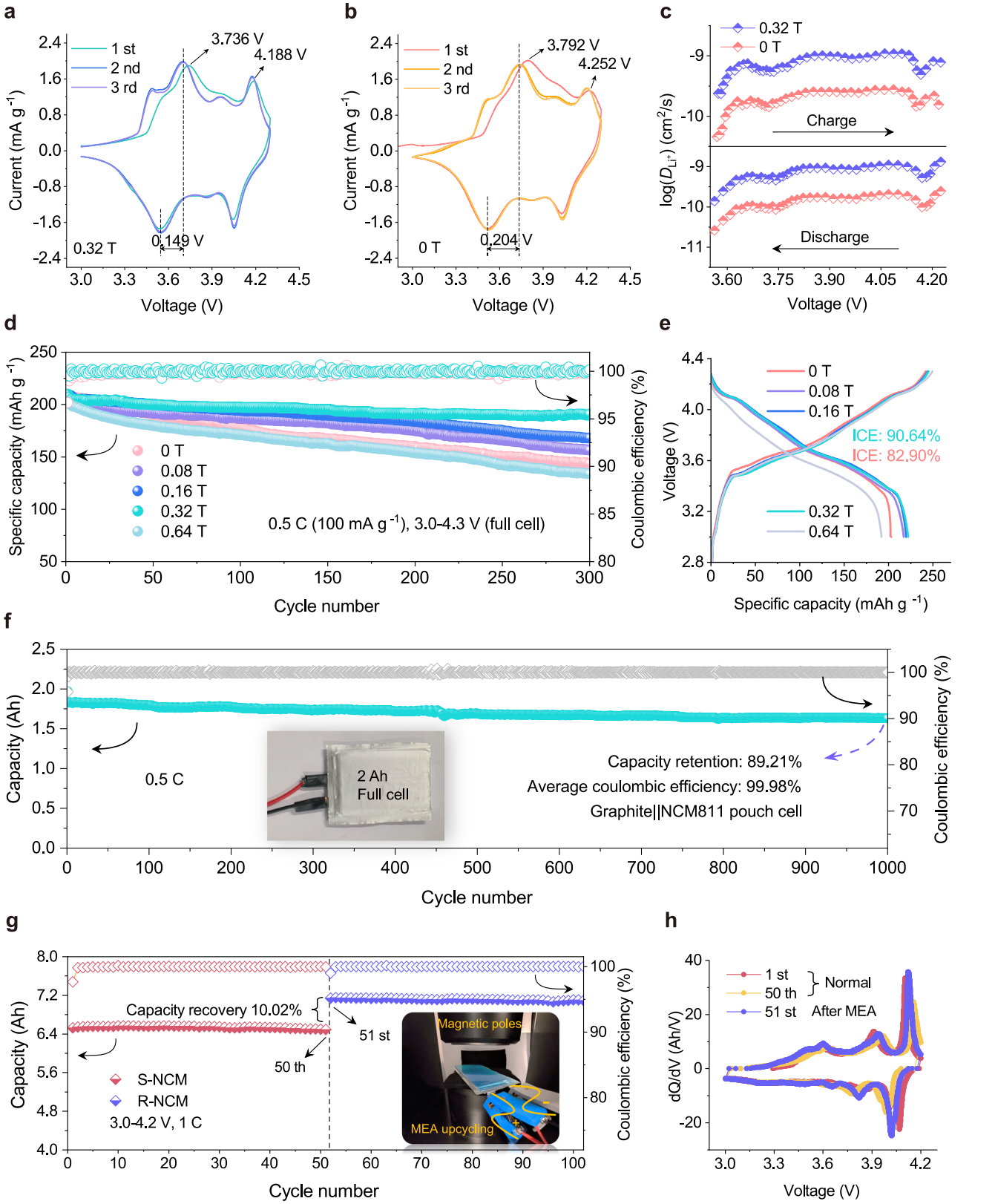

Fig. 4 | Electrochemical performance of NCM811. a, **b** CV curves of the 0.32 T and 0 T MEA graphite | |NCM811 full battery at 0.1 mV/s over the potential range of 3.0–4.3 V. **c** Lithium-ion diffusion coefficient (D_{Li}^{+}) at the first cycle (charge and discharge) after the initial activation in the graphite||NCM811 full battery. **d** Cycling performance of graphite||NCM811 full batteries activated in different magnetic fields (0, 0.08, 0.16, 0.32, 0.64 T). 1 C = 200 mA g^{-1}, and the mass loading of the positive electrode material is 14–15 mg cm^{-2}. **e** The initial activation curves corresponding to (**d**). **f** The cycle performance at 0.5 C of the 2.0 Ah graphite||NCM811 pouch cell with the 0.32 T MEA in the first cycle. **g** The upcycling performance of the spent commercial SiC||NCM811 pouch cell at 1 C between 3.0 and 4.2 V. **h** dQ/dV curves corresponding to the spent-NCM (S-NCM) and regenerated-NCM (R-NCM).

electrode (22.5 g/cm^2) and graphite negative electrode (18.6 g/cm^2) and performed by the same treatment of MEA for initial cycle at 0.1 C within the potential range of 3.0–4.3 V (Fig. 4f). After the ordered rearrangement of Ni ions in 0.32 T magnetic field, the graphite|| NCM811 pouch cell exhibits a high specific energy of 288.75 Wh/kg at 0.9 A. After 1000 cycles, it maintains an 89.21% capacity retention at 0.5 C. In addition, the 0.32 T MEA pouch cell displays a high average Coulombic efficiency of 99.985 ± 0.019%. The specific energy is calculated based on the total mass of the pouch cell, and the detailed parameters are listed in Supplementary Table 4.

We further investigated the magneto-electrochemical synergistic effect on the spent SiC||NCM811 pouch cell (S-NCM, nominal capacity 8 Ah) which was restored by means of larger magnetic poles with 0.32 T and cycled between 3.0 and 4.2 V (Fig. 4g). The capacity of rejuvenated SiC||NCM811 (R-NCM) increased by 10.02% and exhibited excellent cycle reversibility and stability (Fig. 4g, h and Supplementary Fig. 13). Notably, the voltage hysteresis associated with the lithiation/delithiation process was significantly mitigated after the rejuvenation. Assessing the disorder degree in degraded NCM811 before and after repair, we observed that the magneto-electrochemical synergy can also rejuvenate the Ni/Li cation orderliness in spent NCM811 (Supplementary Figs. 14 and 15). Different from the pyrometallurgical and hydrometallurgical recycling methods, the actual operation of MEA recovery method requires negligible costs, mainly including equipment depreciation, time expenditure and electricity, as illustrated in Supplementary Fig. 16. The MEA regeneration pathway excels in sustainability and energy efficiency for recycling end-of-life batteries, owing to its minimal resource consumption and straightforward process. Comparative analysis of the current recycling methods is detailed in Supplementary Fig. 16. The MEA regeneration stands out for its high value-added products and convenient operating procedures, particularly in the field of rejuvenating NCM811-based batteries. In addition, this route is also superior in wastewater management, gas emissions, and operation simplicity, avoiding the complex disposal procedures. Consequently, the MEA regeneration route is possible for the future recycling industry.

The improved kinetics of MEA batteries

The 0.32 T MEA graphite||NCM811 battery shows an excellent high-rate performance (Fig. 5a) with reversible capacities of 218.4, 198.5, 185.6, 168.5, 153.7, and 118.8 mAh g^{-1} at 0.1, 0.5, 1, 2, 3, and 5 C, respectively, while the 0 T MEA graphite||NCM811 battery displays low capacities of 212.74, 195.01, 177.91, 120.49, 71.03, and 50.90 mAh g^{-1}, respectively (Fig. 5b). In Fig. 5c, the 0.32 T MEA battery delivers a high reversible discharge capacity at 5 C and retrieves steadily to the corresponding capacity of 192.1 mAh g^{-1} at 0.5 C. Compared with the control sample (0 T), the enhanced high-rate ability can be ascribed to the persistent and stable ionic channels, which heavily depend on the stability of orderly rearrangement layered oxide.

To clarify the influence of MEA on the structural evolution after cycling, high-resolution transmission electron microscopy tests of 0.32 T and 0 T MEA-NCM811 were also conducted, respectively. After 300 cycles, the 0.32 T MEA-NCM811 still maintained the integrity of its layered structure (Fig. 5d), attributed to the initial reconstruction and the highly ordered Ni/Li cation rearrangement by MEA. In Fig. 5e, the Ni/Li antisite disorder leads to an uneven phase transition, from internal layered structure to external disordered and inactive rock salt phase[24]. In order to explore the influence of the structural change of NCM811 on the kinetic performance after cycling, the electrochemical impedance spectroscopy (EIS) was further examined to analyze the detailed electrochemical reaction kinetics (Fig. 5f, g). The σ value of 0.32 T MEA-NCM811 is about 259.3 after 300 cycles (Fig. 5h and Supplementary Eqs. 9 and 10). This value of 0 T MEA-NCM811 is much higher than that in 0.32 T MEA-NCM811, suggesting that 0.32 T MEA-NCM811 maintains an enhanced Li^+ diffusion coefficient after cycling.

The effect on cathode|electrolyte interface

EIS and corresponding fitted impedance values for the batteries are presented in Fig. 6a, b and Supplementary Table 5. Compared with the control cell (0 T), the impedances of MEA-cells decrease gradually with magnetic intensities augmenting, and attain the minimum at 0.32 T. Typically, at room temperature (25 °C), the charge transfer resistance (R_{ct}) and surface film resistance (R_{sf}) of 0.32 T MEA-NCM811 are 46.8 and 8.1 Ω, respectively, much lower than those of 0 T MEA-NCM811 (83.7 Ω for R_{ct} and 11.9 Ω for R_{sf}). It indicates that the electronic transmission and the Li^+ diffusion are enhanced with the increase of the Ni/Li cation ordered arrangement, which is influenced by the magnetic field intensity.

Fitting EIS data to the equivalent circuit model at multiple frequencies, we applied the Arrhenius law (Supplementary Eqs. 11 and 12) to calculate the activation energy after cycling, revealing the dynamics of lithium-ion transfer at both the interface and in the bulk phase (Fig. 6c, d and Supplementary Table 6). The Li^+ interface migration energy barriers are 43.1 kJ mol^{-1} (0.32 T) and 46.2 kJ mol^{-1} (0 T), respectively. Moreover, the energy barrier for Li^+ diffusion in the bulk phase of 0.32 T MEA-NCM811 (52.4 kJ mol^{-1}) is substantially lower compared with the control sample (62.3 kJ mol^{-1}). The decreased activation energy, attributed to the MEA effect, enhances the electrochemical reaction kinetics. Additionally, this improvement also indicates a continuous and ordered lithium-ion diffusion channel within the layered oxide.

As shown in Fig. 6e, f, scanning electron microscope (SEM) images reveal the structural integrities of NCM811 activated by different method after 300 cycles. When it was activated by MEA (0.32 T), there was no obvious crack due to the intact layered structure. In the case of the control sample, the several surface cracks were caused by the severe tensile/extrusion stress accumulation and inhomogeneity within the particles, exacerbating the deterioration of mechanical properties. High Ni/Li antisite disorder predisposes NCM811 to phase transition, and the severe surface cracks exacerbate this situation by triggering continuously irreversible side reactions.

Figure 6g shows the adsorption energies and electronic states of electrolyte components absorbed at NCM811 surfaces (Supplementary Fig. 17). The adsorption of $LiPF_6$ (−0.840 eV) and EC (−1.630 eV) at the ordered NCM811 is obviously stronger than that at the disordered NCM811 ($LiPF_6$ −0.669 eV, EC −1.390 eV). Furthermore, the highest occupied molecular orbital energy levels of the adsorbed species ($LiPF_6$, EC) at the ordered NCM811 are elevated relative to the disordered NCM811, and both of them are higher than free $LiPF_6$ (−8.985 eV) and EC (−6.934 eV). Density functional theory (DFT) calculations reveal that the highly ordered NCM811 surface presents an abundance of Ni–O sites, facilitating the adsorption of fluoride (*F) and oxide (*O) species and catalyzing the formation of the CEI. In addition, the results of X-ray photoelectron spectroscopy (XPS) in Supplementary Fig. 18 certifies that the optimal MEA condition (0.32 T) promotes CEI to generate more LiF and organic carbonate than the control sample (Supplementary Tables 7 and 8). The peak of Ni 2*p* at 831.08 eV is almost inexistence in the SEI on graphite for MEA battery (Supplementary Fig. 19 and Table 9), suggesting the inhibition of nickel dissolution.

Discussion

In summary, we explored a noninvasive “rejuvenation” strategy of Nickel-rich NCM-based battery via MEA to enhance its electrochemical performance. The advantages of this strategy are threefold. (i) Magnetic field realizes the transition of Ni in metastable NCM811 from high-spin to low-spin state, and thus decreases the super-exchange interaction of Ni–O–TM, meanwhile electrochemical reaction leads to the Ni-ion ordered rearrangement and the structural rejuvenation. (ii) The rejuvenated layered structure enhances the integrity of micron-sized bulk

https://doi.org/10.1038/s41467-024-54641-z

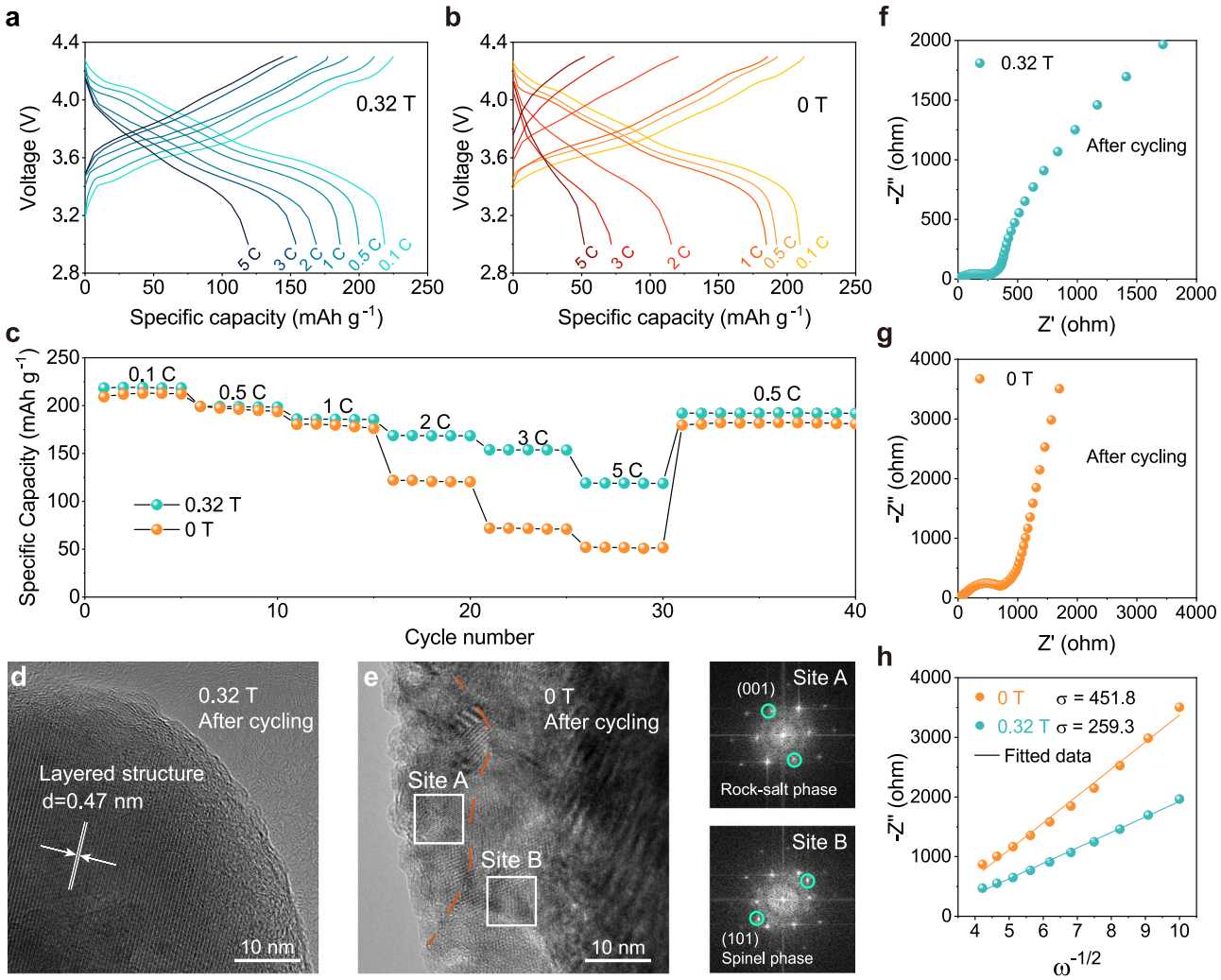

Fig. 5 | Dynamic of the graphite||NCM811 full battery. a, **b** Charge and discharge curves at the rate of 0.1 C, 0.5 C, 1 C, 2 C, 3 C, and 5 C. **c** The rate retention curves. **d**, **e** High-resolution TEM images of 0.32 T and 0 T MEA-NCM811 after 300 cycles and the corresponding FFT patterns (the selected region site A for the surface and the site B for the interior area) of (**e**). **f**, **g** EIS Nyquist diagrams of 0.32 T and 0 T MEA-NCM811 after 300 cycles. **h** The relationship between the angular frequency $\omega^{-1/2}$ and −Z″ from the low-frequency regions in (**f**, **g**).

configuration and refrains from the intergranular cracking. (iii) The surface modification, derived from spin state control and structural rejuvenation, promotes the generation of compact and stable CEI, which is crucial for long-term stability. Furthermore, MEA is a facile, green, and economic strategy, which can function as a pretreatment way of unique energy transmission behavior in initial electrochemical activation or rejuvenation process. Consequently, our study provides insights into the sustainable utilization and regenerative techniques for NCM-based batteries, highlighting their broad applicability and promising prospects for industrial adoption.

Methods

Material preparation

Commercial NCM811 (the nominal composition is $LiNi_{0.83}Co_{0.07}Mn_{0.10}O_2$) and graphite (Guizhou Zhenhua E-Chem Co., LTD) were utilized as the positive and negative electrode material to investigate the activation process of various magnetic intensity on electrochemical performance. To prepare the positive electrode, the active material was mixed with super carbon and polyvinylidene fluoride (weight ratio 90: 5: 5) in N-methyl-2-pyrrolidone (NMP). Then the slurry was cast onto aluminum foil with a 250 μm scraper and dried overnight in a vacuum oven at 100 °C. The positive electrode plate was cut into round pieces with a diameter of 12 mm, and the mass loading of the active material was about 15 mg cm^{-2} for the full cell test. The obtained positive electrode sheets were dried overnight in a vacuum oven at 50 °C before assembling. The corresponding graphite negative electrode was prepared with 80 wt% active material, 10 wt% polyvinylidene fluoride and 10 wt% carbon black in NMP and coated on the copper current collector. 2032-type coin cells were assembled to test their electrochemical performance, in which NCM811 was used as positive electrode, graphite as negative electrode, Celgard-2025 with a diameter of 16 mm as separator and 1 M $LiPF_6$ in ethylene carbonate and diethyl carbonate (EC:DEC = 3:7 by volume) was used as an electrolyte. Add 40 μL electrolyte on both sides of the separator. The coin cells assembled in a glove box filled with argon, where the moisture and oxygen content were controlled below 0.5 ppm.

Magneto-electrochemical synergistic activation and electrochemical tests

The assembled battery was equilibrated at room temperature (25 °C) for 12 h in the absence of the magnetic field. Subsequently, the MEA

https://doi.org/10.1038/s41467-024-54641-z

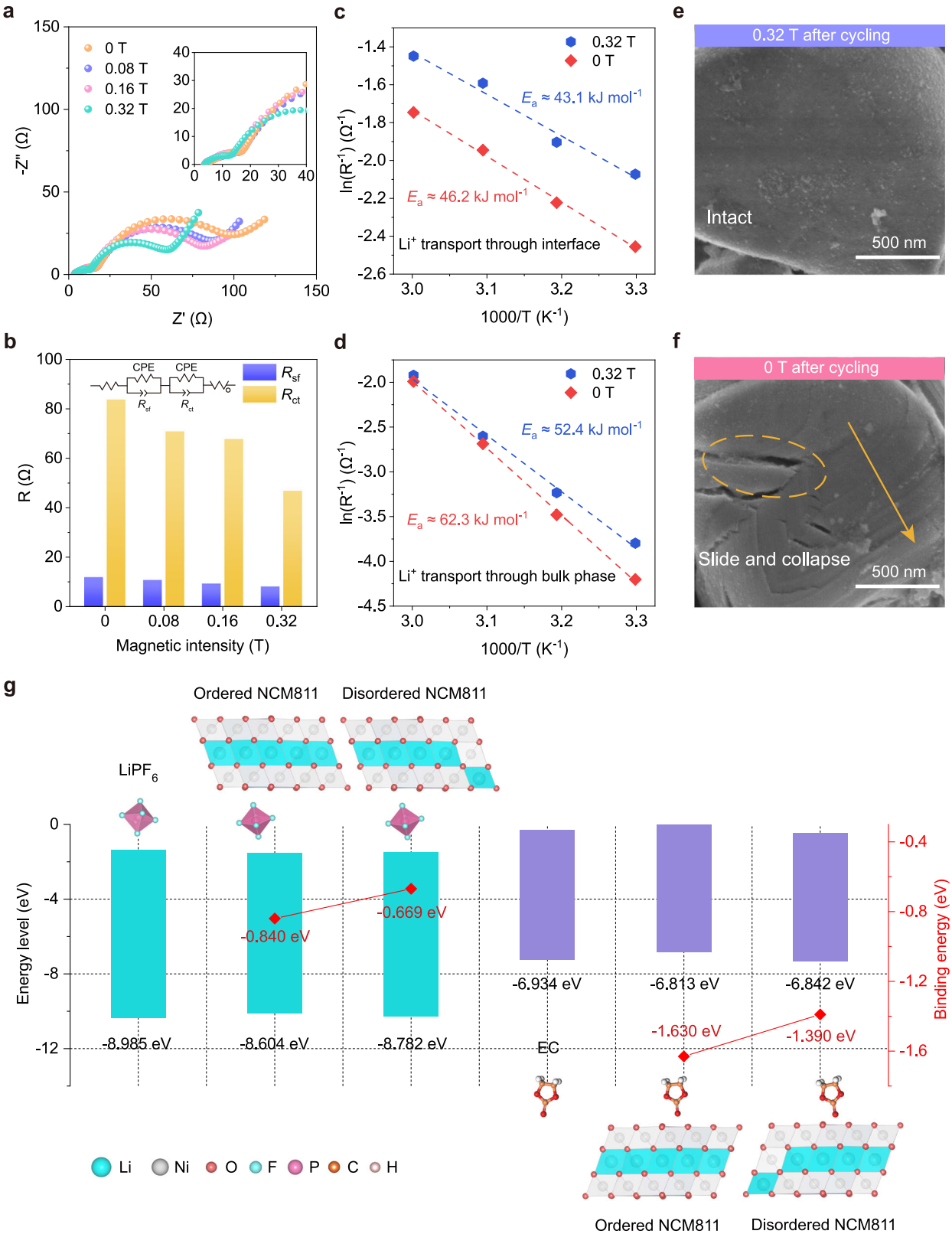

Fig. 6 | Characterization and formation mechanism of CEI in the graphite‖NCM811 full battery. a Electrochemical impedance spectroscopy (EIS) for batteries activated in various magnetic intensities (0, 0.08, 0.16, 0.32 T) for the first cycle, with the inset showing the high-frequency region EIS for the four conditions. **b** The corresponding R_{sf} (surface film resistance), R_{ct} (charge transfer resistance) measured from the results of EIS. **c**, **d** Activation energy of interface reaction and charge transfer process. The activation energies were calculated by the classic Arrhenius law according to the EIS results at different temperatures (303 K, 313 K, 323 K, 333 K). **e**, **f** SEM images of 0.32 T MEA-NCM811 and 0 T MEA-NCM811 surface after 300 cycles, respectively. **g** The energy levels and binding energy of $LiPF_6$ and EC adsorbed at ordered NCM811 and disordered NCM811, respectively.

experiment of coin and pouch cells was conducted at 25 °C between 3.0 and 4.3 V, utilizing a low current density of 0.1 C (Land CT-2001A) and the support of electromagnets.

The magnetic field was generated using the parallel electromagnets from YP Magnetic Technology Development Co., Ltd. With the excitation power supply, an adjustable and uniform magnetic field can be generated between the two pole caps, in which the direction of the magnetic field is along the axial direction of the pole caps. For testing in the magnetic field, the coin/pack cells are sandwiched between two magnets. The magnetic field intensity, which is determined by the output power and the pole gap width, can be continuously adjusted from 0 T to 1.6 T. Here, we use the Tunkia Tesla meter to accurately measure the magnetic field intensity.

The galvanostatic current charging and discharging performance is achieved by assembling the prepared samples into CR-2032 button cell, and on the Neware battery cycler system, the voltage range is 3.0–4.3 V (vs. Li^+/Li) at 0.5 C (1 C = 200 mA g^{-1}). Ivium electrochemical workstation was utilized to characterize the CV curves (sweep rate: 0.1 mV s^{-1}, voltage window: 3–4.3 V), while a CHI660 electrochemical workstation was used for Electrochemical impedance spectra tests (frequency range: 100,000–0.01 Hz). All the electrochemical test was carried out under ambient temperature (~25 °C, the temperature error is 3 °C).

Material characterization

XRD (Bruker D8-Focus with Cu Kα radiation, λ = 1.5418 Å) was used to examine the crystal structure of NCM811 cathode with different charging states and powder. The scanning rate was 5° min^{-1}, and the range of 2θ was between 10° and 80°. Microstructures and morphology of samples were characterized by field emission SEM (FEI Apreo S LoVac and HITACHI S4800), and field emission transmission electron microscope (TEM, JEM-F2100). Chemical composition of CEI was measured by XPS (Thermo-Fisher Scientific) with Al Kα radiation source and depth profiles were obtained by assisted Ar^+ etching. The energy of XPS data was calibrated according to the C 1*s* spectra at 284.8 eV. Before XPS measurement, the cycled samples were washed three times with dimethyl carbonate (DMC) to remove the residual electrolyte salt. The magnetism of materials was studied by the superconducting quantum interference design magnetometer (MPMS-XL). The M–T curves were recorded in the temperature range of 2–300 K under a magnetic field of 1 T. Two modes: zero field cooling (ZFC) and field cooling (FC) are used to determine the magnetic behavior. In this study, there was no difference in ZFC and FC measurements of all samples. EPR spectra were obtained on a Bruker A300 spectrometer operated at 300 K.

Further explanation of sample pretreatment and transfer details is provided as follows. The activated battery (or NCM811 powder) was meticulously disassembled within the glove box to prevent exposure to ambient atmosphere. Subsequently, any residual lithium salts adhering to the surface were meticulously removed by DMC. The electrode material was then carefully peeled off, and its mass was precisely measured and recorded for subsequent analysis. The sample was carefully encapsulated in a waterproof polymer film while housed within the argon-filled glove box to maintain an inert atmosphere. For magnetic measurements, the sample holder was meticulously transferred from the protective argon environment to a vacuum chamber, ensuring that the sample was not exposed to air throughout the whole transition process.

Theoretical calculation

The spin-polarized calculations were carried out using the Vienna ab initio simulation package with the projector augmented-wave pseudopotential for the core electrons and the Perdew–Burke–Ernzerhof (PBE) for exchange–correlation functional. The energy and force convergence criteria for electronic and ionic interaction were set to be 10^{-5} eV and 0.02 eV $Å^{-1}$, respectively. The effective U values (U–J) were set as 4.5, 4.9, and 6.0 eV for Mn, Co, Ni based on a previous study, respectively. A symmetrical 4 × 4 supercell with 20 Å vacuum space was used to avoid the interaction between periodic adsorbed molecules and the Γ-centered k-point density of the Brillouin zone was set to 0.03 $Å^{-1}$ using Monkhorst–Pack grid. The disorder energy of one pair of Ni and Li ions is defined as:

$$E = E_{total}(Ni_{Li}) - E_{total}$$

where $E_{total}(Ni_{Li})$ is the total energy of the supercell with one Ni-ion disorder in Li site, and E_{total} is the total energy of the supercell without Ni/Li antisite disorder.

DFT was used to examine the configuration and binding energy between NCM811 and electrolyte components in the PBE of generalized gradient approximation. During the geometry optimization process, all the atom positions were allowed to relax. To ensure consistent convergence criteria for all the models, a cutoff energy of 500 eV for the plane wave basis, an energy relaxation of 1×10^{-5} eV per atom, a force relaxation of 0.03 eV $Å^{-1}$ and the maximum displacement of 0.001 Å were employed. The Grimme method for DFT-D correction was added to calculate van der Waals interaction. The supercell sizes were set to 5 × 5 × 3 for nickel-rich NCM model. The structural model of disordered NCM811 was set up by exchanging one Li atom with a Ni atom. After that, (003) lattice plane was cleaved with a vacuum space of 20 Å, which was adopted to avoid the interaction between the bounding layers.

The cluster adsorption energy (E_{ad}) for cluster molecules in various slabs was defined according to the equation:

$$E_{ad} = E_{tot} - E_{a1} - E_{a2}$$

where E_{tot} is the total energy of the binding system, E_{a1} is the energy of the optimized clean surface slabs and E_{a2} is the energy of the adsorbates in vacuum.

Data availability

The data that support the plots within this paper and other findings of this study are available from the corresponding author on request. Source data are provided with this paper. Source data are also available at Figshare: [https://doi.org/10.6084/m9.figshare.27314499].

References

1. Larcher, D. & Tarascon, J. M. Towards greener and more sustainable batteries for electrical energy storage. *Nat. Chem.* **7**, 19–29 (2015).
2. Li, W., Erickson, E. M. & Manthiram, A. High-nickel layered oxide cathodes for lithium-based automotive batteries. *Nat. Energy* **5**, 26–34 (2020).
3. Kwade, A. et al. Current status and challenges for automotive battery production technologies. *Nat. Energy* **3**, 290–300 (2018).
4. Schmuch, R., Wagner, R., Hörpel, G., Placke, T. & Winter, M. Performance and cost of materials for lithium-based rechargeable automotive batteries. *Nat. Energy* **3**, 267–278 (2018).
5. Lee, W. et al. Advances in the cathode materials for lithium rechargeable batteries. *Angew. Chem. Int. Ed.* **59**, 2578–2605 (2020).
6. Jung, R. et al. Nickel, manganese, and cobalt dissolution from Ni-rich NMC and their effects on NMC622-graphite cell. *J. Electrochem. Soc.* **166**, A378–A389 (2019).
7. Wei, H.-X. et al. Comprehensive understanding of Li/Ni intermixing in layered transition metal oxides. *Mater. Today* **51**, 365–392 (2021).
8. Clément, R. J., Lun, Z. & Ceder, G. Cation-disordered rocksalt transition metal oxides and oxyfluorides for high energy lithium-ion cathodes. *Energy Environ. Sci.* **13**, 345–373 (2020).

9. Flores, E., Novák, P., Aschauer, U. & Berg, E. J. Cation ordering and redox chemistry of layered Ni-rich $Li_xNi_{1-2y}Co_yMn_yO_2$: an operando Raman spectroscopy study. *Chem. Mater.* **32**, 186–194 (2020).
10. Zhang, S. et al. Insights into cation migration and intermixing in advanced cathode materials for lithium-ion batteries. *Adv. Energy Mater.* **14**, 2402068 (2024).
11. Sun, Y.-K. et al. High-energy cathode material for long-life and safe lithium batteries. *Nat. Mater.* **8**, 320–324 (2009).
12. Kim, U.-H. et al. Heuristic solution for achieving long-term cycle stability for Ni-rich layered cathodes at full depth of discharge. *Nat. Energy* **5**, 860–869 (2020).
13. Tan, S. et al. Additive engineering for robust interphases to stabilize high-Ni layered structures at ultra-high voltage of 4.8 V. *Nat. Energy* **7**, 484–494 (2022).
14. Bi, Y. et al. Reversible planar gliding and microcracking in a single-crystalline Ni-rich cathode. *Science* **370**, 1313–1317 (2020).
15. Zheng, J. et al. Role of superexchange interaction on tuning of Ni/Li disordering in layered $Li(Ni_xMn_yCo_z)O_2$. *J. Phys. Chem. Lett.* **8**, 5537–5542 (2017).
16. Mukherjee, P. et al. Sample dependence of magnetism in the next-generation cathode material $LiNi_{0.8}Mn_{0.1}Co_{0.1}O_2$. *Inorg. Chem.* **60**, 263–271 (2021).
17. Lu, S.-Q. et al. Surface lattice modulation through chemical delithiation toward a stable nickel-rich layered oxide cathode. *J. Am. Chem. Soc.* **145**, 7397–7407 (2023).
18. Li, M. & Lu, J. Cobalt in lithium-ion batteries. *Science* **367**, 979–980 (2020).
19. Zheng, J. et al. Ni/Li disordering in layered transition metal oxide: electrochemical impact, origin, and control. *Acc. Chem. Res.* **52**, 2201–2209 (2019).
20. Chen, H., Dawson, J. A. & Harding, J. H. Effects of cationic substitution on structural defects in layered cathode materials LiNiO2. *J. Mater. Chem. A* **2**, 7988–7996 (2014).
21. Ye, T. et al. Magnetic frustration effect on the rate performance of $LiNi_{0.6}Co_{0.4-x}Mn_xO_2$ cathodes for lithium-ion batteries. *Adv. Energy Mater.* **12**, 2201556 (2022).
22. Zhang, G. et al. A monofluoride ether-based electrolyte solution for fast-charging and low-temperature non-aqueous lithium metal batteries. *Nat. Commun.* **14**, 1081 (2023).
23. Huang, W. et al. Revealing roles of Co and Ni in Mn-rich layered cathodes. *Adv. Energy Mater.* **11**, 2102646 (2021).
24. Kang, S., Lee, S., Lee, H. & Kang, Y.-M. Manipulating disorder within cathodes of alkali-ion batteries. *Nat. Rev. Chem.* **8**, 587–604 (2024).
25. Zhu, Y.-P. et al. Observation of plaid-like spin splitting in a non-coplanar antiferromagnet. *Nature* **626**, 523–528 (2024).
26. Jin, Y.-Z. et al. Tuning spin state of rock-salt-based oxides by manipulation of crystallinity for efficient oxygen electrocatalysis. *Adv. Energy Mater.* **8**, 1703469 (2018).
27. Kanamori, J. Superexchange interaction and symmetry properties of electron orbitals. *J. Phys. Chem. Solids* **10**, 87–98 (1959).
28. Chernova, N. A. et al. Layered $Li_xNi_yMn_yCo_{1-2y}O_2$ cathodes for lithium ion batteries: understanding local structure via magnetic properties. *Chem. Mater.* **19**, 4682–4693 (2007).
29. Wu, K. et al. Dynamic evolution of antisite defect and coupling anionic redox in high-voltage ultrahigh-Ni cathode. *Angew. Chem. Int. Ed.* **63**, e202410326 (2024).
30. Zheng, J. et al. Tuning of thermal stability in layered $Li(Ni_xMn_yCo_z)O_2$. *J. Am. Chem. Soc.* **138**, 13326–13334 (2016).
31. Zhu, H. et al. Spontaneous strain buffer enables superior cycling stability in single-crystal Nickel-rich NCM cathode. *Nano Lett.* **21**, 9997–10005 (2021).
32. Nam, K.-W. et al. Combining in situ synchrotron X-ray diffraction and absorption techniques with transmission electron microscopy to study the origin of thermal instability in overcharged cathode materials for lithium-ion batteries. *Adv. Funct. Mater.* **23**, 1047–1063 (2013).
33. Wu, W. et al. Magnetic actuation enables programmable lithium metal engineering. *Adv. Energy Mater.* **12**, 2200999 (2022).
34. Chen, Y., Huang, H., Liu, L., Chen, Y. & Han, Y. Diffusion enhancement to stabilize solid electrolyte interphase. *Adv. Energy Mater.* **11**, 2101774 (2021).

Acknowledgements

This work was supported by the National Key Research and Development Program of China (2022YFA1504102), the National Natural Science Foundation of China (22279089), the Natural Science Foundation of Tianjin (23JCJQJC00300), and the Municipal Key R&D Program of Ningbo (2023Z109).

Author contributions

H.G. and J.S. conceived the idea and designed the experiments. Q.X., C.Z. and J.S. supervised this work and provided financial support. H.G., Y.C., B.Z., Y.Z., S.Z., and C.H. helped establish the equipment and electrochemical tests. X.W., Y.M. and S.L. provided insight into mechanism exploration. J.Z. suggested the material characterization and data analysis. H.G. and H.W. conducted the theoretical calculations. H.G. and Y.C. conducted SEM, TEM, and data analysis. H.G. and J.S. prepared the manuscripts. All authors participated in discussing and approving the final manuscript.

Competing interests

The authors declare no competing interests.

Additional information

Supplementary information The online version contains supplementary material available at https://doi.org/10.1038/s41467-024-54641-z.

Correspondence and requests for materials should be addressed to Jie Sun.

Peer review information *Nature Communications* thanks the anonymous reviewers for their contribution to the peer review of this work. A peer review file is available.